ACS Sustainable Chemistry & Engineering

Research Article

pubs.acs.org/journal/ascecg

Solar-to-Electric Performance Enhancement by Titanium Oxide Nanoparticles Coated with Porous Yttrium Oxide for Dye-Sensitized Solar Cells

Bingxin Zhao,[†] Jinshu Wang,*[,†] Hongyi Li,*[,†] Yue Xu,[†] Haijun Yu,[†] Xinjian Jia,[†] Xiaofei Zhang,[†] and Yaowu Hao[‡]

[†]Key Laboratory of Advanced Functional Materials, College of Materials Science and Engineering, Beijing University of Technology, Beijing 100124, People's Republic of China

[‡]Department of Materials Science and Engineering, University of Texas at Arlington, Arlington, Texas 76019, United States

Supporting Information

ABSTRACT: TiO_2–Y_2O_3 core–shell nanoparticles for dye-sensitized solar cells (DSSCs) have been fabricated by a solvothermal technique. The heterostructure of TiO_2 nanoparticles coated with porous Y_2O_3 is confirmed with transmission electron microscopy. The bonding of the Y_2O_3 coating on the TiO_2 surface is quantitatively analyzed in terms of the Lifshitz–van der Waals and electrostatic contributions to the surface free energy of the particles. TiO_2 and Y_2O_3 constitute a core–shell heterojunction because the Fermi levels merge; this increases the open-circuit voltage. Higher recombination resistances are obtained in DSSCs with porous Y_2O_3-coated TiO_2 compared with those in the reference cells, indicating "backscattering" inhibition of the porous Y_2O_3 barrier on TiO_2 nanoparticles. Moreover, smaller transport resistances and longer electron lifetimes are achieved in DSSCs with TiO_2–Y_2O_3 core–shell nanoparticles. Compared with a reference cell, the V_{OC} of a DSSC with a partial Y_2O_3 coating on the surface of the TiO_2 nanoparticles improves from 683 to 738 mV and the J_{sc} from 14.15 to 15.35 mA·cm^{-2}, whereas the conversion efficiency increases by 15.2%.

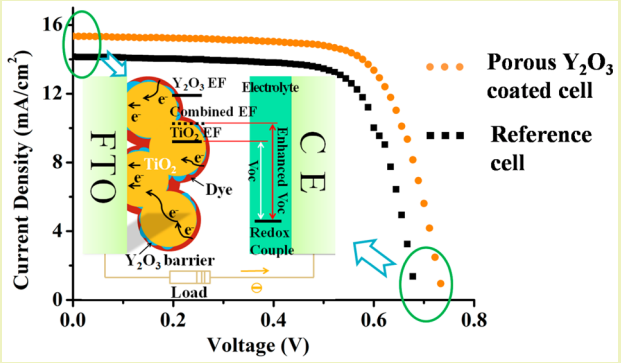

KEYWORDS: *Yttria, Porous coating, Heterojunction, Backscattering barrier, Photovoltage, Photovoltaic performance*

INTRODUCTION

Dye-sensitized solar cells (DSSCs) invented by Grätzel[1] have attracted broad attention with intensive research activities for decades. As one of the most important parts of the DSSC, the photoanode aroused special concerns. Effective electron-transfer and decoupled Fermi levels of the *n*- and *p*-type conductors were the key objectives to get high-quality DSSCs.[2,3] Hence, extremely thin insulating films have been applied to the photoelectrode of DSSCs in the past decade. Grätzel's group[4] has modified TiO_2 photoanodes with thin insulating oxide films consisting of Ga_2O_3, ZrO_2, etc. to inhibit the electron backflow from TiO_2 to the redox electrolyte (I^{3-}). Kay et al.[5] found that modification of the TiO_2 electrode with a very thin film of MgO, Al_2O_3 or Y_2O_3 increased the photovoltage of DSSCs. An Al_2O_3 insulating film fabricated by dipping mesoporous TiO_2 electrodes in aluminum organic solutions led to 35% improvement of the efficiency.[6] Y_2O_3 was also deposited on the TiO_2 electrode to retard the back-transfer of electrons to the electrolyte or to the oxidized dye molecules in DSSCs.[7] However, additional barrier films usually need extra fabrication procedures, which limits their application.

The rare earth element yttrium (Y) has a full 4d orbital, which easily produces several electron configurations,[8] and Y_2O_3 has many advantages such as strong adsorption selectivity,[9] high chemical[10] and thermal stability,[11] large energy band gap (5.8 eV)[12] and a small but non-negligible electronic conductivity.[13,14] Therefore, Y_2O_3 is utilized in many fields such as photocatalysis[8] and luminescence.[10,15] There are several synthesis strategies to incorporate yttrium oxide into metal oxide. TiO_2@ZrO_2@Y_2O_3:Eu phosphor particles were prepared by dispersing TiO_2@ZrO_2 microspheres in an aqueous solution of (Y, Eu)$(NO_3)_3$ for 4 h to form a sol, followed by drying and annealing at 1000 °C for 2 h.[16] Y_2O_3:Eu-coated Y_2O_3 nanoparticles (NPs) for photoluminescence application were fabricated by dispersing Y_2O_3 in a (Y, Eu)$(NO_3)_3$ solution and then firing at 900 °C for 3 h.[17] Both syntheses use nitric acid and apply a high temperature treatment, which make them not particularly attractive.

Received: March 18, 2015
Revised: May 7, 2015
Published: June 4, 2015

DOI: 10.1021/acssuschemeng.5b00221
ACS Sustainable Chem. Eng. 2015, 3, 1518–1525

Advances have recently been made in synthesizing metal oxide/sulfide-coated photoanode material, such as ZnS-coated ZnO for protecting ZnO from acidic dyes,[18] and nanoporous MgO-coated TiO_2 for increasing the specific surface area.[19] However, to our knowledge, the fabrication and utilization of photoelectrodes of TiO_2 particles coated with porous Y_2O_3 for blocking the backcurrent and efficient electron transport have not been reported. In this work, we have made an Y_2O_3–TiO_2 core–shell nanostructure by directly growing nanoporous Y_2O_3 onto TiO_2 NPs. The objective of our work is to obtain an understanding about the role of yttrium oxide in tuning the surface properties of titanium oxide, and in improving the photovoltaic performance of DSSCs. We found that the heterojunction in TiO_2–Y_2O_3 core–shell NPs provided a high photocurrent and high photovoltage in DSSCs, because of the novel core–shell structure that hindered unwanted backcurrent and improved the electron-transfer performance.

EXPERIMENTAL SECTION

Preparation of Blank TiO_2 Nanoparticles. Titanium isopropoxide (25 mL) was slowly dropped into deionized water (100 mL) with ultrasonic cavitation and powerful stirring, followed by repeated filtration and dispersion steps in ethanol and deionized water. Filtered samples were annealed at 500 °C in air to obtain the pure anatase phase as well as to oxidize the organic residuals.

Preparation of Yttria-Coated TiO_2 Nanoparticles. The synthesis of TiO_2–Y_2O_3 core–shell nanoparticles (NPs) is based upon a solvothermal method. Figure 1 is a schematic illustration of the fabrication process of TiO_2–Y_2O_3 core–shell NPs. 2.396 g of as-prepared blank TiO_2 NPs were added to a solution of 8 mL of triethanolamine ($C_6H_{15}NO_3$) (TEOA) in 43 mL of deionized water. Different amounts of yttrium nitrate ($Y(NO_3)_3{\cdot}6H_2O$) (Y^{3+} = 0.56, 0.94, 1.25 or 4.38 mmol) were immediately added into the mixture with powerful stirring. The mixture was transferred into a Teflon-lined autoclave and aged for 24 h at 100 °C. In this heating process, the TEOA uniformly enveloped the TiO_2 NPs. TEOA is a weak Lewis base, so it tends to interact with the Lewis acidic Y^{3+}. Thus, Y^{3+} ions were adsorbed on the surface of TiO_2 NPs in this primary aging process. The homogeneity in the mixture is essential for a uniform coating in the following step. This second heating treatment was performed at 140 °C (72 h) to form yttrium oxide on the surface of the core TiO_2 NPs, because yttrium nitrate is decomposed when the temperature reaches 140 °C.[20] At temperatures >140 °C, the Y_2O_3 tends to aggregate because of homogeneous nucleation. Thus, 140 °C was adopted as the optimum temperature for the synthesis of TiO_2–Y_2O_3 core–shell NPs. The mixture solution was filtrated and the resulting NPs were collected after completion of the reaction. The obtained Y_2O_3-coated TiO_2 NPs were denoted as T@1Y, T@2Y, T@3Y and T@4Y, corresponding to the above-mentioned yttrium nitrate concentrations (0.56, 0.94, 1.25 and 4.38 mmol). For comparison, the same solvothermal procedure was applied to synthesize blank TiO_2 without adding yttrium nitrate.

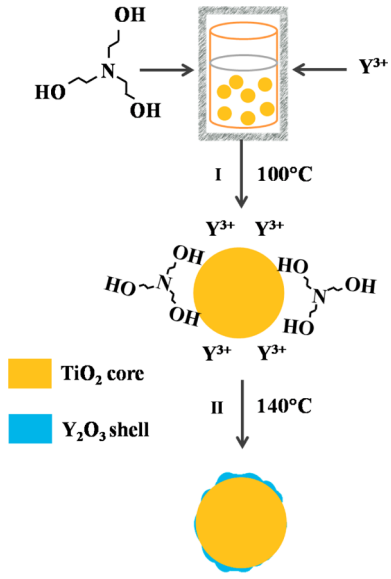

Figure 1. Schematic illustration of the formation of TiO_2–Y_2O_3 core–shell NPs.

Photoanode Preparation. The pastes (Y_2O_3-coated or not) made from the NPs were deposited on the surface of fluorine-doped tin oxide (FTO) conductive glass using the doctor blade technique. The sheet resistance of the FTO was 15 Ω/□. The deposited films were dried at room temperature and then annealed at 500 °C for 2 h in air. The annealed samples were immersed into a solution containing 40 mM $TiCl_4$ for 30 min at 70 °C, rinsed with deionized water and ethanol respectively, and then calcined at 500 °C for 30 min. Finally, the film was dipped into an acetonitrile and ethanol (volume ratio = 2:1) solution containing 0.5 mM *cis*-bis (isothiocyanato)-bis(2,2′-bipyridyl-4,4′-dicarboxylato)-ruthenium(II)-bis-tetrabutyl-ammonium (N719) dye, and kept at 50 °C for 24 h.

Characterizations and Photovoltaic Performance of Yttria-Coated TiO_2 Nanoparticles. The crystal structure of the specimen was identified by X-ray diffraction (XRD) using a Bruker D8 Advance diffractometer with Cu Kα radiation. X-ray photoelectron spectrum (XPS) measurements were performed on X-ray photoelectron equipment made in the UK (ESCALAB 250Xi). The morphology of the obtained samples was studied with transmission electron microscopy (TEM) (FEI Tecnai G2 F30). The current–voltage (I–V) measurements were performed with a Keithley 2400 power source under irradiation of 1 Sun, in which the intensity of the incident light was air mass (AM) 1.5 G. This instrument was equipped with a 300 W solar simulator (Solar Light Co., INC.) that served as the light source. The electrochemical impedance spectrum (EIS) was recorded under dark and illumination conditions via an electrochemical workstation (Zahner, IM6ex).

RESULTS AND DISCUSSION

Investigation of TiO_2–Y_2O_3 Core–Shell Nanoparticles. The XRD diagrams of the as-prepared TiO_2 and TiO_2–Y_2O_3 core–shell nanoparticles (NPs) are shown in Figure 2a. According to JCPDS #65-5714, Figure 2a indicates that blank TiO_2 and T@XY (X = 1, 2, 3, 4) samples exhibit diffraction peaks of the anatase phase. No diffraction peaks of Y_2O_3 can be observed in the T@1Y and T@2Y samples, because the Y_2O_3 content is too low to be detected. The peaks T@4Y at 2θ values of 29.2°, 43.5°, 48.5°, 53.2° and 57.6° can be attributed to the (222), (440), (134), (611) and (622) crystal planes of Y_2O_3 with the cubic structure (JCPDS #65-3178), respectively. However, besides the diffraction peaks from TiO_2 and cubic Y_2O_3, some other diffraction peaks can be observed. A comparison of these other peaks with the information in the JCPDS records was somewhat inconclusive: these peaks are due to an yttrium compound (because of the transformation to cubic Y_2O_3 to be discussed hereafter), but they do not belong to yttrium hydroxide, yttrium nitrate hydroxide or monoclinic Y_2O_3. In Figure 2b, presenting the XRD diffractogram of T@2Y and T@4Y after annealing at 500 °C, the unidentified peaks in Figure 2a have disappeared. This indicates that intermediate Y-compound has completely transformed into cubic Y_2O_3 after sintering. Moreover, the diffraction peaks of cubic yttria became much stronger after calcination, indicating that the crystallinity of cubic Y_2O_3 improved after calcination at 500 °C. Low temperature processing and flame pyrolysis may yield monoclinic crystals: Sotiriou et al.[21] prepared Y_2O_3:Tb^{3+} NPs

DOI: 10.1021/acssuschemeng.5b00221
ACS Sustainable Chem. Eng. 2015, 3, 1518–1525

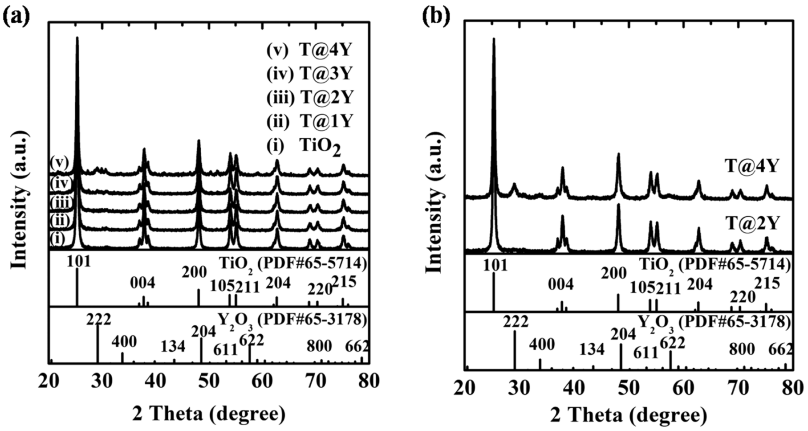

Figure 2. XRD diffractogram of (a) as-prepared TiO_2 and T@XY NPs. (b) T@2Y NPs and T@4Y NPs taken from their photoanode after annealing at 500 °C.

at an annealing temperature of 850 °C for 10 h to get rid of the monoclinic crystal phase. But in our case, the synthesis route does not generate any monoclinic Y_2O_3: this may be due to the solvothermal technique. It can also be seen that the intensities of the anatase peaks of the coated samples become lower compared with pure TiO_2, probably due to the presence of an Y_2O_3 shell on the surface of TiO_2 NPs. The formation of Y_2O_3 in as-prepared NPs was confirmed by X-ray photoelectron spectrum (XPS). As shown in Figure 3b, a comparison of as-

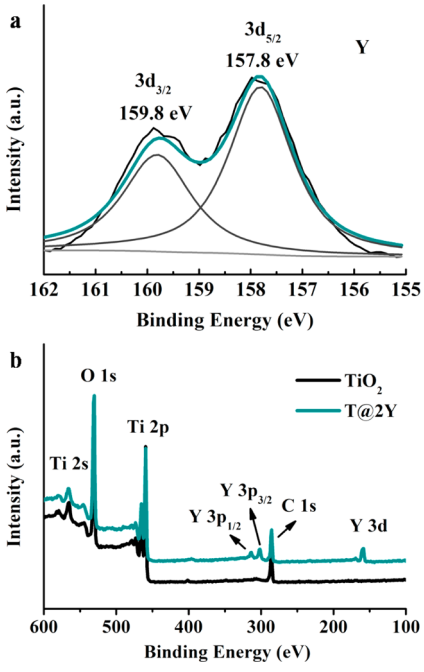

Figure 3. XPS spectrum for (a) Y 3d core levels of T@2Y; the cyan and gray lines are obtained by a curve fitting method. (b) Full scan XPS spectra of blank TiO_2 and T@2Y.

prepared T@2Y with TiO_2 illustrates that the intensity of the Ti peaks of the coated sample slightly decreases probably due to the overlay of Y_2O_3 at the TiO_2 surface. Figure 3a also shows that the binding energies (BE) of the Y $3d_{5/2-3/2}$ doublet of T@2Y are 157.8 and 159.8 eV. These BE values are identical to those earlier reported for the Y_2O_3.[22]

Figure 4 presents TEM images of pure TiO_2, as-prepared T@2Y and NPs taken from the T@2Y photoanode calcined at 500 °C. The particle size of the core−shell structured NPs is in the range of 8−40 nm. Selected area electron diffractions (SAED) are shown as insets in panels a, b and c of Figure 4. The SAED of the reference TiO_2 sample shows anatase. The insets of Figure 4b,c show the polycrystallinity circle of the (222) plane of cubic Y_2O_3: this proves the existence of cubic Y_2O_3 crystallites (JCPDS #65-3178). By comparing Figure 4h with Figure 4i, it can be seen that the crystallinity of the compounds improved after calcination at 500 °C. The grain boundary between TiO_2 and Y_2O_3 can easily be observed in the high-resolution transmission electron microscopy (HRTEM) images of Figure 4e,f. From these images, we derive that the Y_2O_3 shell thickness is 2−4 nm. The image in Figure 4h, which focuses on the core−shell structure of titania and yttria, shows that the lattice spacings for the crystalline planes in the core region are 0.35 and 0.17 nm, corresponding to the (101) and (211) planes of anatase (JCPDS #65-5714), respectively. On the other hand, the interplanar spacing in the shell region is 0.30 nm, corresponding to the (222) plane of yttria (JCPDS #65-3178). The HRTEM image with the Y_2O_3/TiO_2 interface of annealed T@2Y and its corresponding fast Fourier transform (FFT) image are shown in Figure 4i. It can be seen that the Y_2O_3/TiO_2 interface is clean: this creates a strong interfacial bonding. Yttria has a body-centered cubic structure, and anatase has a tetragonal structure. The TiO_2 crystal lattices have *d* spacings of 3.5 and 2.3 Å for the $(01\bar{1})$ plane and $(\bar{1}12)$ planes respectively, as shown in Figure 4i (right), and the related FFT pattern oriented in the [131] direction clearly shows $(01\bar{1})$ diffraction and $(\bar{1}12)$ diffraction. Figure 4i (left) represents cubic Y_2O_3 crystal lattices with a *d* spacing of 2.6 Å for the (040) crystal planes, whereas the corresponding FFT pattern oriented in the [100] direction shows clear {004} diffraction. The interplanar spacing values of the TiO_2 $(\bar{1}12)$ and Y_2O_3 (040) planes are 2.33 and 2.65 Å (JCPDS #65-5714, #65-3178), respectively. These results prove the formation of $TiO_2-Y_2O_3$ core−shell heterostructures. The (040) planes of Y_2O_3 were found to grow epitaxially on the $(\bar{1}12)$ facets of anatase, whereas the lattice misorientation was measured to be ~17°. The formation of $TiO_2-Y_2O_3$ core−shell NPs as discussed above is summarized in Figure 4g. Elemental mapping has been carried out to determine the distribution of Y, Ti and O on the surface of the coating samples. Figure S1 of the Supporting Information (T@2Y) shows that the distribution of O is uniform. Ti is mainly concentrated in the core region, whereas the distribution of Y indicates its presence

DOI: 10.1021/acssuschemeng.5b00221
ACS Sustainable Chem. Eng. 2015, 3, 1518−1525

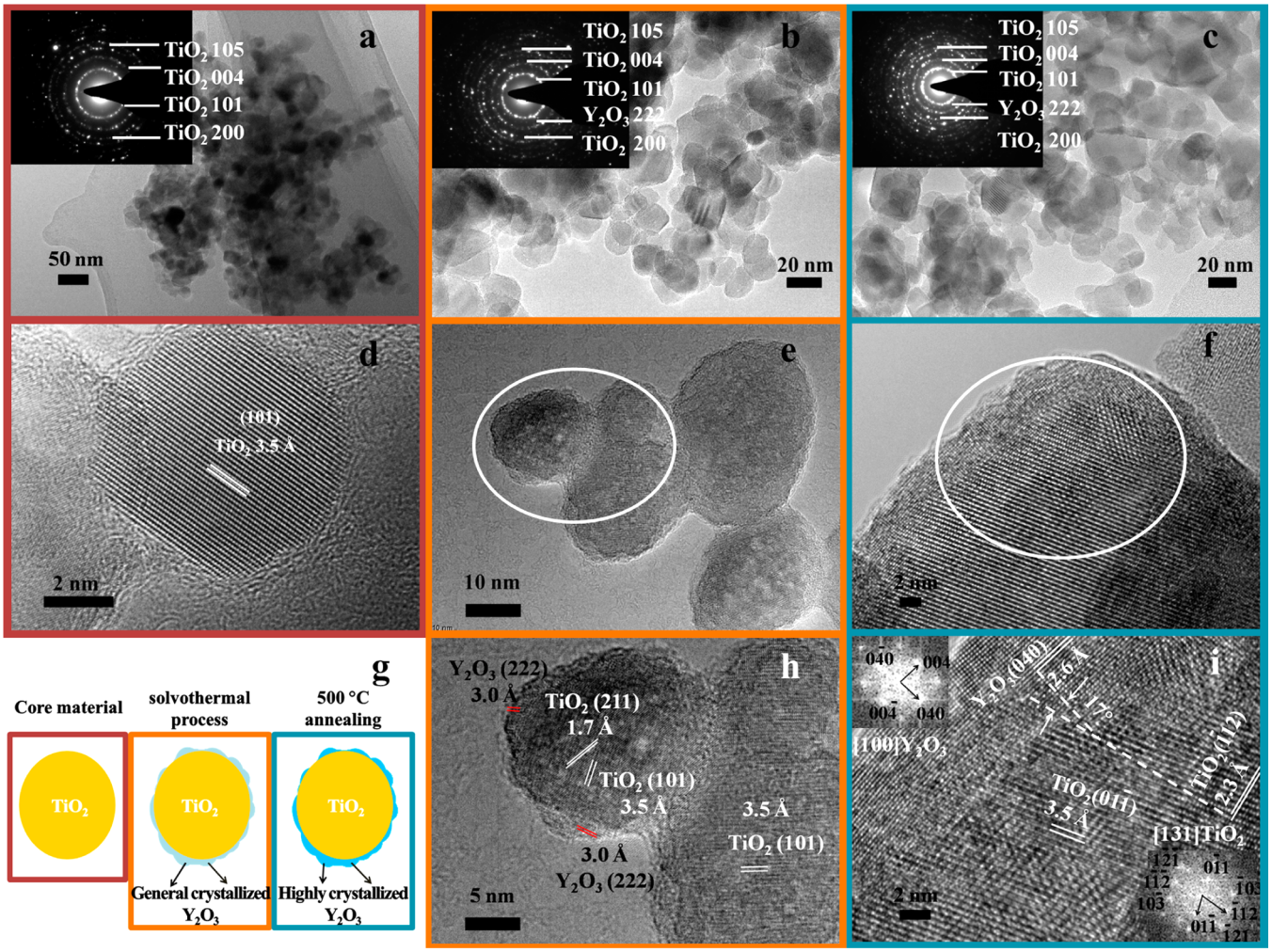

Figure 4. TEM micrographs of TiO_2 (a, d), as-prepared T@2Y NPs (b, e, h), NPs taken from the T@2Y photoanode calcined at 500 °C (c, f, (i) and scheme of Y_2O_3-coated TiO_2 process (g). SAED patterns of each sample are shown as insets in panels a, b and c. The white circle in panels e and f represents the particle location with high-resolution image of T@2Y (h) and annealed T@2Y (i) lattice spacing and planes; the insets in panel i are corresponding FFT patterns.

in the shell. This supports the earlier findings of T@2Y (the Y concentration is 0.94 mmol) that Y_2O_3 grow on the surface of TiO_2 NPs. A TEM micrograph of T@3Y (the Y concentration is 1.25 mmol) is shown in Figure S2a of the Supporting Information. The TiO_2−Y_2O_3 junction can be observed in some regions and the particle size of Y_2O_3 is over 10 nm. The elements distributions of T@3Y displayed in Figure S2b of the Supporting Information indicate the presence of Y in the shell region of NPs, which is also proved by energy dispersive X-ray analysis shown in Figure S2c of the Supporting Information. TEM micrographs of T@4Y (the Y concentration is 4.38 mmol) are shown in Figure S3a−c of the Supporting Information. Apart from the core−shell structure NPs (Figure S3d of the Supporting Information), aggregates of Y_2O_3 nucleation in some region can be observed (Figure S3a of the Supporting Information) and the dimension of Y_2O_3 aggregates are ∼60 nm. It is clear that T@3Y and T@4Y exhibit worse coating effects than T@2Y from the observations above. Therefore, we suppose that T@3Y- and T@4Y-based DSSCs will have worse performance compared with T@2Y-based DSSCs.

To investigate the quality and homogeneity of the Y_2O_3 coating, the surface free energy (SFE) has been calculated from the contact angle (θ) measurements between probing liquids and TiO_2 and T@XY photoanodes annealed at 500 °C. Table S1 of the Supporting Information summarizes γ_L^{LW}, γ_L^+ and γ_L^- for the various probing liquids (water, glycerine and methylene iodide) in mJ/m^2 at 20 °C, which are proposed by van Oss[23] and Lee.[24] The contact angles measured with these probe liquids are shown in Figure S4 of the Supporting Information. The SFE (γ_S) of the NPs is characterized in terms of its two components, the Lifshitz−van der Waals (γ_S^{LW}) and the acid−base or electrostatic (γ_S^{AB}) contribution. γ_S^{AB} is the consequence of the presence of both the electron-donor (γ_S^-) and electron-acceptor (γ_S^+) sites on the solid surface.[9] Young's equation is written as[23]

$$(1 + \cos\theta)\gamma_L^{TOT} = 2\sqrt{\gamma_S^{LW}\gamma_L^{LW}} + 2\sqrt{\gamma_S^+\gamma_L^-} + 2\sqrt{\gamma_S^-\gamma_L^+} \quad (1,)$$

where γ_L^{TOT} is the total surface free energy.

The SFE components of TiO_2 and T@XY NPs are displayed in Table 1. The γ_S^{LW} values of 50.54, 50.62, 50.65, 50.65 and 50.63 $mJ{\cdot}m^{-2}$ are obtained for TiO_2 and T@XY NPs. We note that T@XY NPs show a γ_S^{LW} contribution to their surface free energy that approaches the value of pure Y_2O_3,[9] thus confirming the tight coating of yttria on TiO_2. As is known,

DOI: 10.1021/acssuschemeng.5b00221
ACS Sustainable Chem. Eng. 2015, 3, 1518−1525

Table 1. Surface Free Energy and Its Components of TiO_2 and T@XY NPs

sample	γ_S^{LW}(mJ·m^{-2})	γ_S^+(mJ·m^{-2})	γ_S^-(mJ·m^{-2})
TiO_2	50.54	0.85	55.45
T@1Y	50.62	0.88	55.09
T@2Y	50.65	0.97	54.36
T@3Y	50.65	0.92	54.72
T@4Y	50.63	0.84	54.67

pure anatase is a strong electron donor,[25] and its γ_S^- is higher than that of pure Y_2O_3 (42.9 mJ·m^{-2}).[9] Unlike γ_S^+, the electron-donor component γ_S^- is very sensitive to the surface composition of the core−shell particles.[9] The reduction in γ_S^- brought about by the yttrium oxide shell can be seen in all coated samples: γ_S^- values of pure TiO_2, T@1Y, T@2Y, T@3Y and T@4Y NPs are 55.45, 55.09, 54.36, 54.72 and 54.67 mJ·m^{-2}, respectively. If the TiO_2 NPs are completely coated by Y_2O_3, then the γ_S^- values of the coated samples should be equal to that of Y_2O_3. Hence, the difference in γ_S^- for Y_2O_3-covered TiO_2 and pure Y_2O_3 indicates that the shell is porous. This conclusion is consistent with the TEM results. Among the T@XY NPs, T@2Y NPs have the lowest γ_S^-, indicating the most efficient coating. These are consistent with the elemental mapping results. Furthermore, a systematic increase in specific surface area (SSA) is observed and depicted in Figure S5 and Table S2 of the Supporting Information. This will be favorable for the enhancement of dye-adsorption capability of T@XY photoelectrodes. The T@2Y NPs have the most efficient coating with the largest SSA among the coated samples; therefore, the T@2Y photoelectrode is expected to exhibit a better performance in the photoelectric conversion.

Photovoltaic Performance. *I*−*V* characteristics curves of TiO_2-based DSSC and T@XY-based DSSCs are depicted in Figure 5. A general trend can be observed in the increase of the

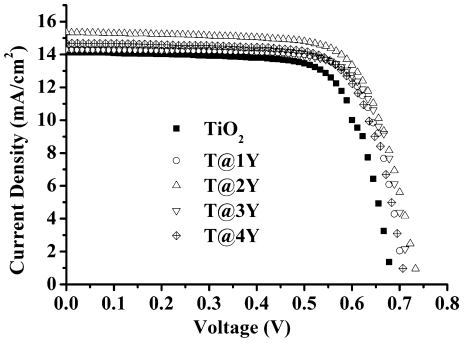

Figure 5. *I*−*V* curves of the DSSC devices based on reference TiO_2 and T@XY.

open circuit voltage (V_{OC}), the short circuit current density (J_{SC}) and the solar-to-electric conversion efficiency. Figure S6 of the Supporting Information is a schematic diagram of the photoinjected electron-transfer of TiO_2 nanoparticles with a complete coating and with a partial/porous coating of Y_2O_3. The photoinjected electrons produced in the excited dye molecule (D^*) may transfer in two ways at the interface of a NP with a nonporous coating: either entering into the TiO_2 by tunneling (shown as panel i in Figure S6a of the Supporting Information) or moving back to the dye after failing to cross the energy barrier of Y_2O_3 (shown as ii in Figure S6a of the Supporting Information). Particles with a porous coating, as shown in Figure S6b of the Supporting Information, enable most photoinjected electrons to transfer from the excited state of the dye into TiO_2 due to the existence of a direct TiO_2/dye interface at the noncoated areas. Therefore, DSSCs with completely coated particles are expected to exhibit worse photovoltaic performance than those with porous coated NPs. Kumara et al.[26] prepared completely insulating oxide coatings on TiO_2 and found that J_{SC} reduced from 9.0 to 7.0 mA/cm^2 after coating. They concluded that the insulating oxide coating hindered both electron injection and electron−hole recombination, which might allow electron tunneling from the TiO_2 core back to the oxidized dye and I_3^- ions in the electrolyte. But in our case, as shown in Figure 5, J_{SC} increases after Y_2O_3 coating due to the porous structure of Y_2O_3. Table 2 lists the V_{OC} values of the DSSCs: coating TiO_2 with Y_2O_3 (T@2Y) improves the from 683 to 738 mV. However, when the concentration of Y ions is higher than 0.94 mmol (initial molar concentration of T@2Y), both the photocurrent and photovoltage of a T@XY-based DSSC decrease due to the formation of extra yttrium oxide nanoparticles during the solvothermal process (Figures S2 and S3 of the Supporting Information).

Electrochemical impedance spectroscopy (EIS) has been applied to study the electron-transfer of photoanodes made of NPs coated with porous Y_2O_3 in more detail. The DSSCs based on TiO_2 and T@XY photoanodes have been measured in a frequency range from 10 mHz to 3 MHz, under dark conditions (Figure 6a) and simulated solar light of 100 mW/cm^2 (Figure 6b). The equivalent circuit is shown in Figure S7 of the Supporting Information. Figure 6a depicts the semicircular curve obtained in the intermediate-frequency regime shows the interfacial charge recombination resistance (R_{ct}) caused by electron transport from the TiO_2 conduction band to the I_3^- ions in the electrolyte.[28] The radius of the intermediate frequency semicircle (Figure 6a) shows a general increase of the T@XY "backscattering" impedance as compared with TiO_2, confirming that Y_2O_3 inhibits back-transfer of injected electrons to the I_3^- ions in the electrolyte. Porous coatings of Y_2O_3 (2−4 nm) at the surface of the anatase particles lead to the increase of the dark reaction impedance of the T@2Y device (67.2 Ω), more than 3 times higher than that of TiO_2 (19.0 Ω). This demonstrates that a porous Y_2O_3 coating on TiO_2 NPs retards the charge recombination between the electrons in the photoelectrode and the holes in the *p*-type organic conductors.

Table 2. Detailed Parameters of T@XY-based DSSCs Devices

DSSC device	film thickness (μm)	V_{OC} (mV)	J_{SC} (mA/cm^2)	FF (%)	eff (%)	R_{ct} (Ω)	R_t (Ω)	ω_{max} (Hz)	τ_e (ms)
TiO_2	10.20	683	14.15	72.52	7.01	19.0	27.67	22.38	7.12
T@1Y	10.10	710	14.29	75.10	7.62	50.8	17.21	22.17	7.18
T@2Y	10.15	738	15.35	71.30	8.08	67.2	14.55	21.81	7.30
T@3Y	9.95	721	14.31	74.31	7.67	61.1	24.32	21.89	7.27
T@4Y	10.15	711	14.70	72.34	7.56	26.8	25.36	24.37	6.53

DOI: 10.1021/acssuschemeng.5b00221
ACS Sustainable Chem. Eng. 2015, 3, 1518−1525

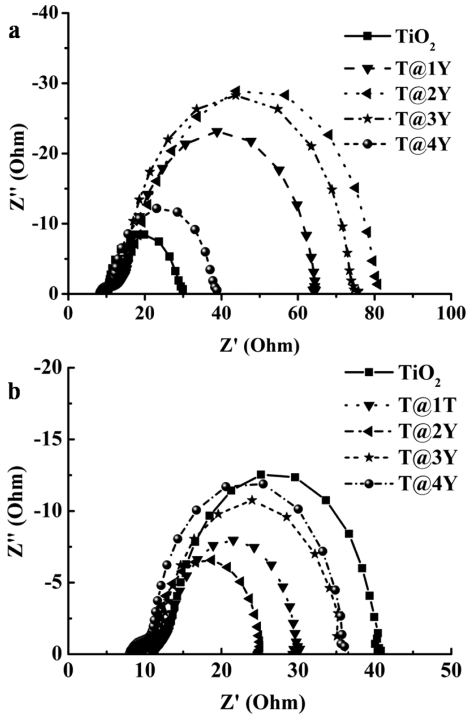

Figure 6. Nyquist plots for DSSCs based on reference TiO_2 and T@XY NPs, measured at a forward bias of 5 mV in (a) dark conditions and (b) light of 100 mW/cm^2 (AM 1.5).

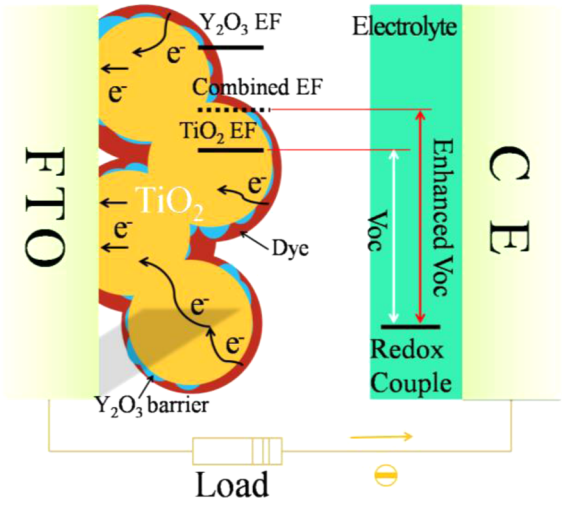

Figure 7. Schematic diagram of the operation principle of TiO_2–Y_2O_3 core–shell NPs-based DSSCs. Energy levels are taken from refs 31 and 32 (see Figure S10 of the Supporting Information).

The semicircle in the intermediate frequencies (Figure 6b) represents the transport resistance (R_t) of electrons within the photoanode and the charge-transfer at the dye–photoanode–electrolyte interface.[28,29] The diameters of the semicircle at medium frequencies become smaller after coating with Y_2O_3, indicating that more efficient charge-transfer processes have taken place at the dye–TiO_2 bilayer/electrolyte interface. The photovoltaic parameters are summarized in Table 2. From this table, it can be concluded that the larger J_{SC} values, induced by larger R_{ct} and smaller R_t values, are caused by the porous Y_2O_3 coating, which reduces the recombination of the photoinjected electrons and holes in the dye/electrolyte (ions) without inhibiting the interfacial electron-transfer. We also measured the incident photocurrent efficiency (IPCE) spectra of the T@XY and reference DSSCs, as shown in Figure S8 of the Supporting Information. The IPCE results indicate that the porous Y_2O_3 coating has better performance in harvesting incident photons: this is consistent with the trend of the photocurrent performance of the DSSCs. Figure S8 of the Supporting Information also demonstrates that the IPCE of DSSCs based on T@2Y is the highest over the whole solar spectrum among all the samples.

Another interesting parameter in DSSCs is the electron lifetime (τ_e), which is defined by the frequency peak (ω_{max}) in the middle arc of Figure S9 of the Supporting Information according to the following equation, $\tau_e = (2\pi\omega_{max})^{-1}$. As shown in Table 2, τ_e increases in the sequence T@2Y > T@1Y > TiO_2 whereas a large decrease in T@4Y occurs due to the aggregation of Y_2O_3 (homogeneous nucleation). Because T@2Y has the lowest transport resistance, highest electron lifetime and highest recombination resistance among the five cells, the most efficient charge-transfer process occurs in T@2Y. The rather high values of the just mentioned parameters for T@2Y also facilitate electron transport over a long distance. Therefore, this cell exhibits the highest J_{SC} of 15.35 mA/cm^2.

To describe the effect of TiO_2@Y_2O_3 NPs on the photovoltaic performance of DSSCs, we present the operation principle in porous Y_2O_3-covered TiO_2 NPs of DSSC in a schematic diagram shown in Figure 7. The conduction band edge of yttrium oxide is significantly more negative than both the TiO_2 conduction band edge (see Figure S10 of the Supporting Information) and the oxidation potential of the excited dye, indicating that Y_2O_3 can function as a barrier layer.[27] The photoinjected-electron-transfer kinetics of the TiO_2@Y_2O_3-based DSSCs has been discussed above in Figure S6 of the Supporting Information. The foregoing considerations may be summarized as follows: the porous Y_2O_3 coating does not reduce the electron injection yield, but rather retards the interfacial charge recombination significantly. The voltage produced under illumination corresponds to the difference between the electron energy in the Fermi energy (EF) level of the wide-band-gap oxide and the electrochemical potential in the hole conductor (electrolyte).[30] Besides, the Fermi level of Y_2O_3 is higher than that of TiO_2.[31,32] Because TiO_2 and Y_2O_3 constitute a heterojunction, the EFs will align after establishing equilibrium.[33,34] In our case, a downward shift in the Fermi energy level of the Y_2O_3 and an upward shift in the Fermi energy level of the TiO_2 will occur, thus raising the Fermi level of T@XY NPs and subsequently the V_{OC} of their DSSCs compared to that with pure TiO_2 NPs and its DSSC.

CONCLUSION

Dye-sensitized solar cells with a photoanode containing TiO_2–Y_2O_3 core–shell nanoparticles were fabricated and showed significantly improved performance. Unlike completely insulating oxide coatings, porous Y_2O_3 shells achieved the desired electron-transfer by repelling the negative charged I_3^- without affecting the interfacial electron-transfer. The experimental results revealed the advantages of the porous Y_2O_3 coating on the TiO_2 particles, such as more efficient charge-transfer, backscattering inhibition and photovoltage enhancement. The porous Y_2O_3 shell structure is an efficient backscattering barrier between TiO_2–dye/electrolyte interfaces, while it enhances

DOI: 10.1021/acssuschemeng.5b00221
ACS Sustainable Chem. Eng. 2015, 3, 1518–1525

charge-transfer at the same time. Furthermore, the core−shell heterostructure combines the Fermi levels of TiO_2 and Y_2O_3. Thus, compared with a reference cell with pure TiO_2 particles, a DSSC with a porous Y_2O_3 coating (T@2Y) shows an increase of open-circuit voltage from 683 to 738 mV, an increase of short-circuit current from 14.15 to 15.35 mA/cm^2 and an increase of the overall device efficiency from 7.01% to 8.08%. We hope that the results of our research work stimulate further research in coating TiO_2 particles for DSSCs, because we believe that there are opportunities for further improvements.

■ ASSOCIATED CONTENT

Supporting Information

Surface energies and polarities of probe liquids, SSA of TiO_2 and T@XY, elemental mapping patterns, energy dispersive X-ray analysis, TEM micrographs, STEM energy dispersive X-ray analysis, surface energies of probe liquids, contact angle measurements, specific surface area, schematic diagram of electron-transfer, IPCE spectra, equivalent circuit for EIS tests, Bode plots of EIS tests and Fermi energy level of TiO_2 and Y_2O_3. The Supporting Information is available free of charge on the ACS Publications website at DOI: 10.1021/acssuschemeng.5b00221.

■ AUTHOR INFORMATION

Corresponding Authors

*J. Wang. E-mail: wangjsh@bjut.edu.cn. Tel./Fax: +8610-67391101.

*H. Li. E-mail: lhy06@bjut.edu.cn. Tel./Fax: +8610-67391101.

Notes

The authors declare no competing financial interest.

■ ACKNOWLEDGMENTS

This work is financially supported by the National Natural Science Foundation of China (51471006, 51225402), the Beijing Natural Science Foundation (2151001) and the Guangxi Natural Science Foundation (2014GXNSFBB118001). We acknowledge Prof. Daniel den Engelsen for the fruitful discussion and the language improvement. We thank Dr. Wenhao Fan (Beijing Centre for Physical & Chemical Analysis) for the TEM measurement.

■ REFERENCES

(1) O'Regan, B.; Grätzel, M. A low-cost, high-efficiency solar cell based on dye-sensitized colloidal TiO_2 films. *Nature* **1991**, *353* (6346), 737−740.

(2) Grätzel, M. Recent advances in sensitized mesoscopic solar cells. *Acc. Chem. Res.* **2009**, *42* (11), 1788−1798.

(3) Ning, Z. J.; Fu, Y.; Tian, H. Improvement of dye-sensitized solar cells: What we know and what we need to know. *Energy Environ. Sci.* **2010**, *3* (9), 1170−1181.

(4) Chandiran, A. K.; Nazeeruddin, M. K.; Grätzel, M. The role of insulating oxides in blocking the charge carrier recombination in dye-sensitized solar cells. *Adv. Funct. Mater.* **2014**, *24* (11), 1615−1623.

(5) Kay, A.; Grätzel, M. Dye-sensitized core-shell nanocrystals: Improved efficiency of mesoporous tin oxide electrodes coated with a thin layer of an insulating oxide. *Chem. Mater.* **2002**, *14* (7), 2930−2935.

(6) Palomares, E.; Clifford, J. N.; Haque, S. A. Control of charge recombination dynamics in dye sensitized solar cells by the use of conformally deposited metal oxide blocking layers. *J. Am. Chem. Soc.* **2003**, *125* (2), 475−482.

(7) Lin, L. Y.; Yeh, M. H.; Chen, C. Y. Surface modification of TiO_2 nanotube arrays with Y_2O_3 barrier layer: Controlling charge recombination dynamics in dye-sensitized solar cells. *J. Mater. Chem. A* **2014**, *2* (22), 8281−8287.

(8) Xu, Y. N.; Gu, Z. Q.; Ching, W. Y. Electronic, structural, and optical properties of crystalline yttria. *Phys. Rev. B* **1997**, *56* (23), 14993−15000.

(9) Plaza, R. C.; Zurita, L.; Durán, J. D. G.; González-Caballero, F.; Delgado, A. V. Surface thermodynamics of hematite/yttrium oxide core-shell colloidal particles. *Langmuir* **1998**, *14* (24), 6850−6854.

(10) Dugandžić, I.; Lojpur, V.; Mančić, L.; Dramićaninb, M. D.; Rabanalc, M. E.; Hashishind, T.; Tand, Z.; Oharad, S.; Milošević, O. Aerosol route as a feasible bottom-up chemical approach for up-converting phosphor particles processing. *Adv. Powder Technol.* **2013**, *24* (5), 852−857.

(11) Hartmanova, M.; Gmucova, K.; Thurzo, I. Dielectric properties of ceria and yttria-stabilized zirconia thin films grown on silicon substrates. *Solid State Ionics* **2000**, *130* (1−2), 105−110.

(12) Kumar, D.; Sharma, M.; Pandey, O. P. Effect of co-doping metal ions (Li^+, Na^+ and K^+) on the structural and photoluminescent properties of nano-sized Y_2O_3:Eu^{3+} synthesized by co-precipitation method. *Opt. Mater.* **2014**, *36* (7), 1131−1138.

(13) Le, S. R.; Zhang, J.; Zhu, X. D.; Zhai, J.; Sun, K. Sintering and electrochemical performance of Y_2O_3-doped barium zirconate with Bi_2O_3 as sintering aids. *J. Power Sources* **2013**, *232* (15), 219−223.

(14) Mudavakkat, V. H.; Noor-A-Alam, M.; Bharathi, K. K.; AlFaify, S.; Dissanayake, A.; Kayani, A.; Ramana, C. V. Structure and AC conductivity of nanocrystalline yttrium oxide thin films. *Thin Solid Films* **2011**, *519* (22), 7947−7950.

(15) Chen, N.; Ji, L.; Du, G. P. Luminescent properties of hybrid nanostructures of ion-exchanged Y_2O_3:Eu^{3+} nanoparticles with 2-thenoyltrifluoroacetone ligands. *J. Lumin.* **2014**, *153*, 259−263.

(16) Sun, J. L.; Gao, X.; He, D. P.; Chen, J.; Meng, X.; Zhang, Q.; Shen, L.; Jiao, H. Functionalized TiO_2@ZrO_2@Y_2O_3:Eu^{3+} core-multishell microspheres and their photoluminescence properties. *Particuology* **2013**, *11* (6), 776−781.

(17) Liu, W. J.; Wang, Y. H.; Zhang, M. Q.; Zheng, Y. Synthesis of Y_2O_3:Eu^{3+} coated Y_2O_3 phosphors by urea-assisted homogeneous precipitation and its photoluminescence properties. *Mater. Lett.* **2013**, *96* (1), 42−44.

(18) Bu, I. Y. Y. Optoelectronics of solution processed core shell zinc oxide nanowire/zinc sulphide heterostructure for dye sensitized solar cell applications. *Microelectron. Eng.* **2014**, *128* (5), 48−52.

(19) Lee, S. W.; Kim, J. Y.; Park, J. S. Preparation of nanoporous MgO-coated TiO_2 nanoparticles and their application to the electrode of dye-sensitized solar cells. *Langmuir* **2005**, *21* (23), 10332−10335.

(20) Unfried, P.; Rossmanith, K.; Blaha, H. Zwei neue basische yttrium-nitrate: $Y(OH)_x(NO_3)_{3-x}\cdot H_2O$ und $YO_{x/2}(NO_3)_{3-x}$ (x=1.5). *Monatsh. Chem.* **1991**, *122* (8−9), 635−644.

(21) Sotiriou, G. A.; Schneider, M.; Pratsinis, S. E. Green, silica-coated monoclinic Y_2O_3:Tb^{3+} nanophosphors: Flame synthesis and characterization. *J. Phys. Chem. C* **2012**, *116* (7), 4493−4499.

(22) Zhang, J.; Li, X.; Wang, Y.; Liu, S. Synthesis and characterization of Y_2O_3 nanoparticles and nanorods in magnetron sputtered Ti-Y alloy films. *Appl. Phys. A: Mater. Sci. Process.* **2013**, *110* (2), 465−470.

(23) van Oss, C. J. *Interfacial Forces in Aqueous Media*; 1st ed.; CRC Press: New York, 1994.

(24) Lee, L. H. Correlation between Lewis acid−base surface interaction components and linear solvation energy relationship solvatochromic α and β parameters. *Langmuir* **1996**, *12* (6), 1681−1687.

(25) Bisquert, J. Chemical capacitance of nanostructured semiconductors: Its origin and significance for nanocomposite solar cells. *Phys. Chem. Chem. Phys.* **2003**, *5* (24), 5360−5364.

(26) Kumara, G.; Tennakone, K.; Perera, V. P. S.; Konno, A.; Kaneko, S.; Okuya, M. Suppression of recombinations in a dye-sensitized photoelectrochemical cell made from a film of tin IV oxide crystallites coated with a thin layer of aluminium oxide. *J. Phys. D: Appl. Phys.* **2001**, *34* (6), 868−873.

(27) Palomares, E.; Clifford, J. N.; Haque, S. A.; Lutz, T.; Durrant, J. R. Control of charge recombination dynamics in dye sensitized solar

DOI: 10.1021/acssuschemeng.5b00221
ACS Sustainable Chem. Eng. 2015, 3, 1518−1525

cells by the use of conformally deposited metal oxide blocking layers. *J. Am. Chem. Soc.* **2003**, *125* (2), 475−482.
(28) Wang, Q.; Moser, J. E.; Grätzel, M. Electrochemical impedance spectroscopic analysis of dye-sensitized solar cells. *J. Phys. Chem. B* **2005**, *109* (31), 14945−14953.
(29) Wang, H. H.; Bhattacharjee, R.; Hung, I. M.; Li, L.; Zeng, R. Material characteristics and electrochemical performance of Sn-doped ZnO spherical-particle photoanode for dye-sensitized solar cells. *Electrochim. Acta* **2013**, *111* (30), 797−801.
(30) Grätzel, M. Dye-sensitized solar cells. *J. Photochem. Photobiol., C* **2003**, *4* (31), 145−153.
(31) Janáky, C.; Rajeshwar, K.; Tacconi, N. R. D. Tungsten-based oxide semiconductors for solar hydrogen generation. *Catal. Today* **2013**, *199*, 53−64.
(32) Robertson, J. Band offsets of wide-band-gap oxides and implications for future electronic devices. *J. Vac. Sci. Technol., B: Microelectron. Nanometer Struct.—Process., Meas., Phenom.* **2000**, *18* (3), 1785−1791.
(33) Kim, C.; Kim, K. S.; Kim, H. Y.; Han, Y. S. Modification of a TiO_2 photoanode by using Cr-doped TiO_2 with an influence on the photovoltaic efficiency of a dye-sensitized solar cell. *J. Mater. Chem.* **2008**, *18* (47), 5809−5814.
(34) Zhang, Z.; Shao, C.; Li, X.; Zhang, L.; Xue, H.; Wang, C.; Liu, Y. Electrospun nanofibers of ZnO-SnO_2 heterojunction with high photocatalytic activity. *J. Phys. Chem. C* **2010**, *114* (17), 7920−7925.

DOI: 10.1021/acssuschemeng.5b00221
ACS Sustainable Chem. Eng. 2015, 3, 1518−1525